10.1115/PVP2020-21667

Proceedings of the ASME 2020
Pressure Vessels & Piping Conference
PVP2020
July 19-24, 2020, Minneapolis, Minnesota, USA

PVP2020-21667

A 3D PARALLEL HIGH-ORDER SOLVER WITH CURVED LOCAL MESH REFINEMENT FOR PREDICTING ARTERIAL FLOW THROUGH VARIED DEGREES OF STENOSES

Kuangxu Chen[*] **Bin Zhang**[†] **Chunlei Liang**[‡]
Department of Mechanical and Aeronautics Engineering
Clarkson University
Potsdam, NY, 13699

ABSTRACT

A 3D parallel high-order spectral difference (SD) solver with curved local mesh refinement is developed in this research to simulate flow through stenoses of varied degrees (50%, 60%, 65%, 70% and 75%) of radius constriction at inlet Reynolds number of 500. This solver employs high-order curved mesh in the vicinity of arterial wall and the local mesh refinement technique reduces the overall computational cost by distributing more elements in critical regions. In simulation of flow through stenosis of 50% radius constriction, velocity profiles predicted from the SD solver agree well with previous DNS results and experimental data. Mesh independency study shows that numerical results from a conforming and a non-conforming mesh agree well with each other. When the constriction degree is larger than 50%, visualizations through iso-surfaces of Q-criterion show that vortex rings are ejected from the stenosis throat, advecting downstream before they hit the vessel walls and they finally break down and merge into a large bulk region of small-scale turbulence. The observations are consistent with the vorticity contour which is characterized by development of the Kelvin-Helmholtz instability when shear layers were formed, rolled up and advected downstream between the central jet and the recirculation region. When the constriction degree turns to 75%, the flow transitions rapidly downstream of stenosis throat and dramatic pressure drop is witnessed. This provides a fluid-dynamic explanation for clinical definition of critical stenosis (i.e. over 75% luminal radius narrowing). Furthermore, the pressure drop across a stenosis is found to be proportional to square of ratio of non-stenosed area to minimum area at the stenotic throat with a linear correlation coefficient equal to 0.9998. Finally, this solver is proven to have excellent scalability on massively parallel computers when multi-level refinement of meshes is performed to capture small-scale structures in the turbulence region.

INTRODUCTION

Peripheral arterial occlusive disease (PAD) is prevalent nowadays in the United States, especially among senior citizens. Clinically, doctors define the severity of PADs by the degree of narrowing of stenotic lesion. For example, critical stenoses are empirically characterized by over 75% luminal radius narrowing. The critical stenosis can very often cause turbulence and reduce flow by means of viscous head losses and flow choking. Very high shear stresses near the throat of the stenosis can activate platelets and thereby induce thrombosis, which can severely block blood flow to the heart or brain [1]. Therefore interventional measures such as balloon angioplasty, stent placement, or arterial bypass surgery are usually conducted in patients once narrowing degree reaches 75% [2] . However, the clinical definition of the critical stenosis is still short of a scientific explanation from the perspective of fluid mechanics. In order to accurately and efficiently simulate arterial flow with varied degrees of stenotic constriction, we have developed a high-order SD solver

[*]PhD student, kuchen@clarkson.edu.
[†]Research Assistant Professor, bzhang@clarkson.edu
[‡]Professor, corresponding author, cliang@clarkson.edu

with local mesh refinement capability.

In this contribution, we report a detailed study on the onset of transition in the flows through varied degrees of stenoses with steady inlet velocity. The same stenosis geometry has been a subject of studies of transition to turbulence under steady [3–5], pulsatile [5, 6] and oscillatory [7] flow conditions. All aforementioned studies were performed with a stenosis of 50% radius constriction (or namely 75% area reduction) and mentioned some conditions that can trigger the onset of transition. In [3], introduction of a geometric perturbation, in the form of a stenosis eccentricity that was 5% of the main vessel diameter at the throat, resulted in breaking of the symmetry of the post-stenotic flow field and the flow transitioned to turbulence about five diameters away from the stenosis. In [5], the pulsatile flows became unstable through a subcritical period-doubling bifurcation involving alternating tilting of the vortex rings that were ejected from the throat with each pulse. The present work focuses on simulations of flow through varied degrees of stenoses. The goal is to depict the coherent flow structures in post-stenotic regions when geometries of stenoses change and verify whether the clinical definition of the critical stenosis can be explained by dramatic pressure drop induced by the breakdown of the jet and flow instabilities.

Although structure of the post-stenotic flow field changes dramatically when the degree of radius constriction increases, the effect of geometry of the stenosis on the pressure drop can be expressed in a linear dependency, as reported in [8]. Numerical results in this study prove that this dependency will not change even if the post-stenotic flow transitions and becomes unsteady. This linear relation is useful for prediction of pressure loss across a severe stenosis. Accurate prediction of the pressure loss is important since the reduced pressure distal to the stenosis significantly alters the blood flow to the peripheral beds supplied by the artery [8].

MATHEMATICAL FORMULATION

Spectral Difference Method (SD)

Consider the unsteady 3D compressible Navier-Stokes equations in conservative form

$$\frac{\partial \mathbf{Q}}{\partial t} + \frac{\partial \mathbf{F}}{\partial x} + \frac{\partial \mathbf{G}}{\partial y} + \frac{\partial \mathbf{H}}{\partial z} = \mathbf{0}, \tag{1}$$

where the $\mathbf{Q}$ is the vector of conserved variables; $\mathbf{F}$, $\mathbf{G}$ and $\mathbf{H}$ are the total fluxes including both inviscid and viscous flux vectors with the following expressions,

$$\mathbf{Q} = [\rho \quad \rho u \quad \rho v \quad \rho w \quad E]^T, \tag{2}$$

$$\mathbf{F} = \mathbf{F}_{inv}(\mathbf{Q}) + \mathbf{F}_{vis}(\mathbf{Q}, \nabla\mathbf{Q}), \tag{3}$$

$$\mathbf{G} = \mathbf{G}_{inv}(\mathbf{Q}) + \mathbf{G}_{vis}(\mathbf{Q}, \nabla\mathbf{Q}), \tag{4}$$

$$\mathbf{H} = \mathbf{H}_{inv}(\mathbf{Q}) + \mathbf{H}_{vis}(\mathbf{Q}, \nabla\mathbf{Q}), \tag{5}$$

where ρ is fluid density, u, v and w are x, y and z velocities, E is the total energy per volume defined as $E = p/(\gamma-1) + \frac{1}{2}\rho(u^2+v^2+w^2)$, p is pressure, γ is the ratio of specific heats. The inviscid fluxes and viscous fluxes are

$$\mathbf{F}_{inv} = \begin{pmatrix} \rho u \\ \rho u^2 + p \\ \rho uv \\ \rho uw \\ (E+p)u \end{pmatrix}, \mathbf{G}_{inv} = \begin{pmatrix} \rho v \\ \rho uv \\ \rho v^2 + p \\ \rho vw \\ (E+p)v \end{pmatrix}, \mathbf{H}_{inv} = \begin{pmatrix} \rho w \\ \rho uw \\ \rho vw \\ \rho w^2 + p \\ (E+p)w \end{pmatrix}, \tag{6}$$

and

$$\mathbf{F}_{vis} = -\begin{pmatrix} 0 \\ \tau_{xx} \\ \tau_{yx} \\ \tau_{zx} \\ u\tau_{xx} + v\tau_{yx} + w\tau_{zx} + \frac{\mu C_p}{Pr} T_x \end{pmatrix}, \tag{7}$$

$$\mathbf{G}_{vis} = -\begin{pmatrix} 0 \\ \tau_{xy} \\ \tau_{yy} \\ \tau_{zy} \\ u\tau_{xy} + v\tau_{yy} + w\tau_{zy} + \frac{\mu C_p}{Pr} T_y \end{pmatrix}, \tag{8}$$

$$\mathbf{H}_{vis} = -\begin{pmatrix} 0 \\ \tau_{xz} \\ \tau_{yz} \\ \tau_{zz} \\ u\tau_{xz} + v\tau_{yz} + w\tau_{zz} + \frac{\mu C_p}{Pr} T_z \end{pmatrix}, \tag{9}$$

where τ_{ij} is the shear stress tensor which is related to velocity gradients as $\tau_{ij} = \mu(u_{i,j} + u_{j,i}) + \lambda\delta_{ij}u_{k,k}$, and μ is the dynamic viscosity, $\lambda = -2/3\mu$ based on Stokes' hypothesis, δ_{ij} is the Kronecker delta, C_p is the heat capacity at constant pressure, Pr is the Prandtl number, and T is the temperature.

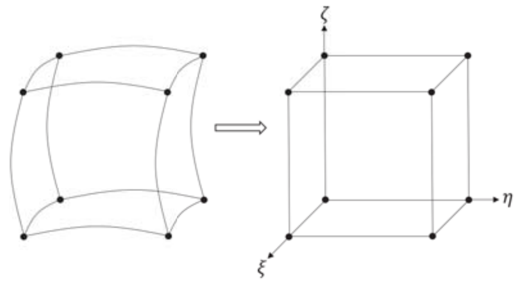

FIGURE 1: TRANSFORMATION FROM PHYSICAL DOMAIN TO COMPUTATIONAL DOMAIN

To achieve an efficient implementation, all elements in the physical domain (x,y,z) are transformed into a computational domain $(0 \le \xi \le 1, 0 \le \eta \le 1, 0 \le \zeta \le 1)$ as shown in Fig. 1. The transformation can be written as:

$$\begin{pmatrix} x \\ y \\ z \end{pmatrix} = \sum_{i=1}^{K} M_i(\xi,\eta,\zeta) \begin{pmatrix} x_i \\ y_i \\ z_i \end{pmatrix}, \tag{10}$$

where K is the number of nodes per element, (x_i, y_i, z_i) are the nodal cartesian coordinates, and $M_i(\xi,\eta,\zeta)$ is the shape function at the $i-$th node. After this transformation, the conservation law is expressed in the computational domain as

$$\frac{\partial \tilde{\mathbf{Q}}}{\partial t} + \frac{\partial \tilde{\mathbf{F}}}{\partial \xi} + \frac{\partial \tilde{\mathbf{G}}}{\partial \eta} + \frac{\partial \tilde{\mathbf{H}}}{\partial \zeta} = \mathbf{0}, \tag{11}$$

where $\tilde{\mathbf{Q}} = |J|\,\mathbf{Q}$ and

$$\begin{pmatrix} \tilde{\mathbf{F}} \\ \tilde{\mathbf{G}} \\ \tilde{\mathbf{H}} \end{pmatrix} = |J| J^{-1} \begin{pmatrix} \mathbf{F} \\ \mathbf{G} \\ \mathbf{H} \end{pmatrix}. \tag{12}$$

The Jacobian matrix J takes the following form

$$J = \frac{\partial(x,y,z)}{\partial(\xi,\eta,\zeta)} = \begin{bmatrix} x_\xi & x_\eta & x_\zeta \\ y_\xi & y_\eta & y_\zeta \\ z_\xi & z_\eta & z_\zeta \end{bmatrix}. \tag{13}$$

In the standard computational element, two sets of points are defined, namely the solution points and the flux points, as illustrated in Fig. 2. In order to construct a degree $(N-1)$ polynomial in each coordinate direction, N solution points in each direction are required. In each dimension, the solution points are chosen as the Chebyshev-Gauss points defined as

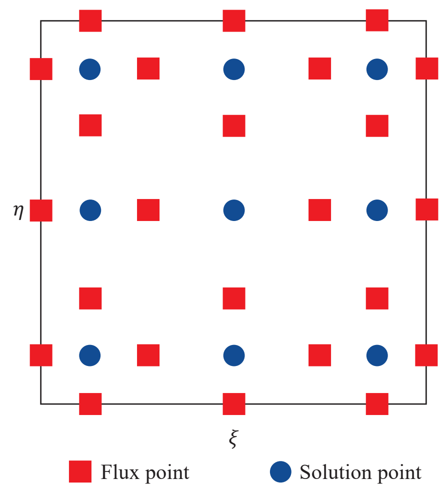

FIGURE 2: SCHMATIC OF THE DISTRIBUTION OF SOLUTION POINTS AND FLUX POINTS FOR A THIRD-ORDER SD SCHEME ON A QUADRILATERAL ELEMENT

$$X_s = \frac{1}{2}[1 - \cos(\frac{2s-1}{2N}\pi)], \quad s = 1,2,\cdots,N. \tag{14}$$

The flux points are chosen as Legendre-Gauss quadrature points plus the two end points 0 and 1. Choosing $P_{-1}(\xi) = 0$ and $P_0(\xi) = 1$, the higher-degree Legendre polynomials can be determined by

$$P_n(\xi) = \frac{2n-1}{n}(2\xi - 1)P_{n-1}(\xi) - \frac{n-1}{n}P_{n-2}(\xi). \tag{15}$$

The Legendre-Gauss quadrature points are the roots of the equation $P_n(\xi) = 0$.

Using the solutions at N solution points, a degree $(N-1)$ polynomial can be built using the following Lagrange basis defined as

$$h_i(X) = \prod_{s=0,s\ne i}^{N} (\frac{X - X_s}{X_i - X_s}). \tag{16}$$

Similarly, using the fluxes at $(N+1)$ flux points, a degree N polynomial can be built for the flux using a similar Lagrange basis defined as:

$$l_{i+1/2}(X) = \prod_{s=0,s\ne i}^{N} (\frac{X - X_{s+1/2}}{X_{i+1/2} - X_{s+1/2}}). \tag{17}$$

The reconstructed solution for the conserved variables in the standard element is just the tensor products of the three one-dimensional polynomials,

$$\mathbf{Q}(\xi,\eta,\zeta)=\sum_{k=1}^{N}\sum_{j=1}^{N}\sum_{i=1}^{N}\frac{\tilde{\mathbf{Q}}_{i,j,k}}{|J_{i,j,k}|}h_i(\xi)\cdot h_j(\eta)\cdot h_k(\zeta), \qquad (18)$$

Similarly, the flux polynomials are constructed as

$$\tilde{\mathbf{F}}=\sum_{k=1}^{N}\sum_{j=1}^{N}\sum_{i=0}^{N}\tilde{\mathbf{F}}_{i+1/2,j,k}l_{i+1/2}(\xi)\cdot h_j(\eta)\cdot h_k(\zeta), \qquad (19)$$

$$\tilde{\mathbf{G}}=\sum_{k=1}^{N}\sum_{j=0}^{N}\sum_{i=1}^{N}\tilde{\mathbf{G}}_{i,j+1/2,k}h_i(\xi)\cdot l_{j+1/2}(\eta)\cdot h_k(\zeta), \qquad (20)$$

$$\tilde{\mathbf{H}}=\sum_{k=0}^{N}\sum_{j=1}^{N}\sum_{i=1}^{N}\tilde{\mathbf{H}}_{i,j,k+1/2}h_i(\xi)\cdot h_j(\eta)\cdot l_{k+1/2}(\zeta). \qquad (21)$$

The above constructed solution and fluxes are only element-wise continuous, but discontinuous across element interfaces. For the inviscid flux, the Rusanov solver [9] is employed to compute a common flux at interfaces to ensure conservation and stability. The derivatives of the inviscid fluxes are computed at the solution points using the derivatives of Lagrange operator l:

$$\left.\frac{\partial\tilde{\mathbf{F}}}{\partial\xi}\right|_{i,j,k}=\sum_{r=0}^{N}\tilde{\mathbf{F}}_{r+1/2,j,k}\cdot l'_{r+1/2}(\xi_i), \qquad (22)$$

$$\left.\frac{\partial\tilde{\mathbf{G}}}{\partial\eta}\right|_{i,j,k}=\sum_{r=0}^{N}\tilde{\mathbf{G}}_{i,r+1/2,k}\cdot l'_{r+1/2}(\eta_j), \qquad (23)$$

$$\left.\frac{\partial\tilde{\mathbf{H}}}{\partial\zeta}\right|_{i,j,k}=\sum_{r=0}^{N}\tilde{\mathbf{H}}_{i,j,r+1/2}\cdot l'_{r+1/2}(\zeta_k). \qquad (24)$$

To numerically handle viscous effect, an averaging approach is used [10–12].

Time Integration Scheme

All computations in this paper are advanced in time using a third-order strong-stability-preserving five-stage Runge-Kutta scheme (SSPRK(5,3)). It is written in the form of Eqn. (25).

$$\begin{aligned}\mathbf{Q}^{(0)}&=\mathbf{Q}^n,\\ \mathbf{Q}^{(i)}&=\sum_{k=0}^{i-1}[\alpha_{ik}\mathbf{Q}^k+\Delta t\beta_{ik}\mathbf{R}(\mathbf{Q}^k)],\quad i=1,2,\cdots,s, \qquad (25)\\ \mathbf{Q}^{(n+1)}&=\mathbf{Q}^s,\end{aligned}$$

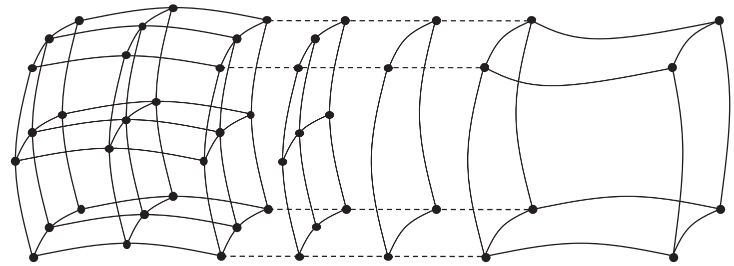

FIGURE 3: SCHEMATICS OF GEOMETRICALLY NON-CONFORMING ELEMENTS WHERE THE LEFT ELEMENT IS SUBDIVIDED INTO EIGHT CHILD ELEMENTS

where $\mathbf{R}=-\frac{\partial\mathbf{F}}{\partial x}-\frac{\partial\mathbf{G}}{\partial y}-\frac{\partial\mathbf{H}}{\partial z}$ is the residual and $s=5$ for a five-stage Runge-Kutta scheme. The coefficients α_{ik} and β_{ik} are taken from the table of SSPRK(5,3) in Ruuth [13]. Non-dimensional time-step $\Delta t u_i/D=5\times10^{-5}$ is used for all cases .

Curved Non-conforming Interface Approach

Local mesh refinement of a hexahedral element will make an originally conforming mesh non-conforming. This means that two elements might share a partial edge or face. Geometrically non-conforming elements require a modification of the usual method to couple them. A conservative approach was introduced in [14] where the surface fluxes were computed on a separate mortar space and then projected back onto the element surfaces. This method was later extended by [15] for curved sliding mesh application and also applied to deal with 3D rotating geometries [16]. This paper uses the watertight mortar algorithm for non-conforming interfaces in a locally refined hexahedral mesh to capture the detailed flow field in the post-stenotic region.

The present implementation will generate non-conforming interfaces when an element is refined to 8 child elements while their neighboring elements are not, as represented in Fig. 3. Specifically, for 20-node isoparametric hexahedral elements, the watertight condition [17] can be preserved during this refinement as long as each child element employs mid-edge nodes of its parent element as its own nodal points, uses quarter-edge nodes of its parent element as its own mid-edge nodes. Maintaining watertight property for non-conforming meshes means that neighboring elements may only share partial face but they represent the same polynomial and there are no gaps in between [17].

Mortars are the intersections of child faces and the corresponding parent faces. Since child faces are parts of parent faces, mortars formed here are identical to child faces. For curved mortar algorithm, parent and child faces are all mapped from physical space to square faces (i.e., $0\leq\xi,\eta\leq1$) in computational space. Meanwhile, mortars are mapped to square mortar faces (i.e., $0\leq\xi',\eta'\leq1$) in the mortar space. This is achieved via

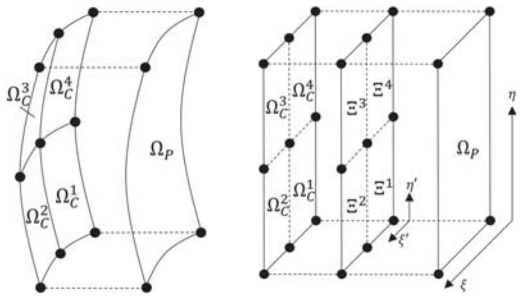

(a) PHYSICAL SPACE (b) COMPUTATIONAL SPACE

FIGURE 4: REPRESENTATION OF PARENT AND CHILD FACES AND MORTARS

2D isoparametric mapping. Schematics of the parent and child faces and mortars shown in physical and computational spaces are Fig. 4a and 4b, where Ω represents an element face, Ξ represents a mortar, subscripts 'C' and 'P' represents child and parent, superscripts are numbers of child faces and mortars. The computational space and mortar space are related as

$$\xi = o_\xi + s_\xi \xi', \quad \eta = o_\eta + s_\eta \eta', \tag{26}$$

where o_ξ and o_η are the offsets of a mortar with respect to the corresponding element face in two coordinate directions, and s is the scaling. For the example shown in Fig. 4, since child face and mortar are identical, offsets of a mortar with respect to child face are all 0 and scalings are all 1. For parent faces, for example, we have $o_\xi^1 = 0$, $s_\xi^1 = L_{\xi'}^{\Xi^1}/L_\xi^{\Omega_P} = 0.5$ for Ξ^1, $s_\xi^2 = L_{\xi'}^{\Xi^2}/L_\xi^{\Omega_P} = 0.5$, $o_\xi^2 = L_{\xi'}^{\Xi^1}/L_\xi^{\Omega_P} = 0.5$ for Ξ^2, where L denotes the physical length of the edge of the face or the mortar and the subscript indicates the coordinate direction which the edge aligns with.

According to Eqn. (18), the solution on Ω_P can be represented as,

$$\mathbf{Q}^{\Omega_P}(\xi,\eta) = \sum_{j=1}^{N}\sum_{i=1}^{N} \mathbf{Q}_{i,j}^{\Omega_P} h_i(\xi) h_j(\eta), \tag{27}$$

where $\mathbf{Q}_{i,j}^{\Omega_P}$ represents the discrete solution at the (i,j)-th solution point on Ω_P, h_i and h_j are the Lagrange bases defined in Eqn. (16). If we define the same set of solution points on $0 \le \xi' \le 1$, $0 \le \eta' \le 1$ for each mortar, then solution on each mortar can be reconstructed similarly,

$$\mathbf{Q}^{\Xi^k}(\xi',\eta') = \sum_{j=1}^{N}\sum_{i=1}^{N} \mathbf{Q}_{i,j}^{\Xi^k} h_i(\xi') h_j(\eta'), \qquad k = 1,2,3,4, \tag{28}$$

where $\mathbf{Q}_{i,j}^{\Xi^k}$ is the solution at the (i,j)-th solution point on a mortar Ξ.

To get the solutions on Ξ^k, we require that

$$\int_0^1 (\mathbf{Q}^{\Xi^k}(\xi',\eta') - \mathbf{Q}^{\Omega_P}(\xi,\eta)) h_\alpha(\xi') h_\beta(\eta') = 0, \qquad \alpha,\beta = 1,2,\cdots,N. \tag{29}$$

Substituting Eqns. (26)-(28) into the above equation and evaluating it at each solution point on Ξ^k will give a system of linear equations. The solution of this system when written in matrix form is

$$\mathbf{Q}^{\Xi^k} = \mathbf{P}^{\Omega_P \to \Xi^k} \mathbf{Q}^{\Omega_P} = \mathbf{M}^{-1} \mathbf{S}^{\Omega_P \to \Xi^k} \mathbf{Q}^{\Omega_P}, \tag{30}$$

where $\mathbf{P}^{\Omega_P \to \Xi^k} = \mathbf{M}^{-1}\mathbf{S}^{\Omega_P \to \Xi^k}$ is the projection matrix from Ω_P to Ξ^k. The matrices $\mathbf{M}$ and $\mathbf{S}^{\Omega_P \to \Xi^k}$ have the following expressions,

$$\mathbf{M} = \int_0^1 \int_0^1 h_\alpha(\xi') h_\beta(\eta') h_i(\xi') h_j(\eta') d\xi' d\eta', \qquad \alpha,\beta,i,j = 1,2,\cdots,N, \tag{31}$$

$$\mathbf{S}^{\Omega_P \to \Xi^k} = \int_0^1 \int_0^1 h_\alpha(\xi') h_\beta(\eta') h_i(o_\xi^k + s_\xi^k \xi') h_j(o_\eta^k + s_\eta^k \eta') d\xi' d\eta', \quad \alpha,\beta,i,j = 1,2,\cdots,N, \tag{32}$$

where o and s are the offset and scaling of Ξ^k with respect to Ω_P and the coordinate subscript indicates the direction.

Note that the projection matrix will reduce to the identity matrix on the side of child faces. After obtaining solutions of both sides of a mortar, the Rusanov solver is employed to compute the common inviscid flux $\mathbf{F}_{inv}^{\Xi}$. This common flux is then transformed to the computational flux as $\tilde{\mathbf{F}}_{inv}^{\Xi}$ according to Eqn. 12. To project the common inviscid fluxes back to parent face Ω, we require that,

$$\sum_{k=1}^{4} \int_{\eta=o_\eta^k}^{\eta=o_\eta^k+s_\eta^k} \int_{\xi=o_\xi^k}^{\xi=o_\xi^k+s_\xi^k} ((\mathbf{F}_{inv}^{\Omega_P}(\xi,\eta) - \mathbf{F}_{inv}^{\Xi^k}(\xi',\eta')) h_\alpha(\xi) h_\beta(\eta) d\xi d\eta = 0, \quad \alpha,\beta = 1,2,\cdots,N, \tag{33}$$

where $\mathbf{F}_{inv}^{\Omega_P}(\xi,\eta)$ is the inviscid flux polynomial on parent face Ω_P. Solution of the above equation when written in matrix form is

$$\begin{aligned}\tilde{\mathbf{F}}_{inv}^{\Omega_P} &= \sum_{k=1}^{4} \mathbf{P}^{\Xi^k \to \Omega_P} \tilde{\mathbf{F}}_{inv}^{\Xi^k} \\ &= \sum_{k=1}^{4} s_\xi^k s_\eta^k \mathbf{M}^{-1} \mathbf{S}^{\Xi^k \to \Omega_P} \mathbf{F}_{inv}^{\Xi^k},\end{aligned} \tag{34}$$

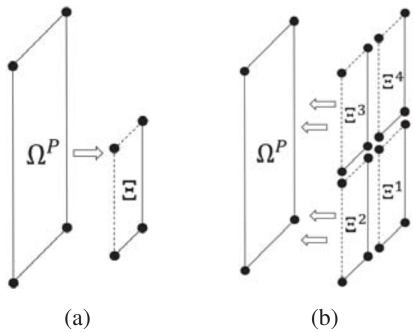

FIGURE 5: PROJECTION BETWEEN PARENT FACE AND MORTARS: (a) FROM PARENT FACE TO MORTAR, (b) FROM FOUR MORTARS BACK TO PARENT FACE.

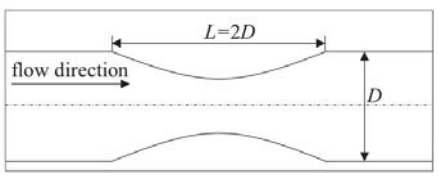

FIGURE 6: SIDE VIEW OF THE STENOSIS GEOMETRY; x IS THE STREAMWISE DIRECTION WHILE y AND z ARE THE CROSS-STREAM DIRECTIONS.

where the matrix $\mathbf{M}$ is identical to that in Eqn. 31, and matrices $\mathbf{S}^{\Xi^k \to \Omega_P}$ $(k = 1,2,3,4)$ are simply transposes of $\mathbf{S}^{\Omega_P \to \Xi^k}$.

The computation of viscous fluxes follows the same procedure. More details can be found in a previous paper [16].

PROBLEM FORMULATION

Flow through axisymmetric stenosis models with steady inlet velocity with geometries corresponding to radius constriction of 50%, 60%, 65%, 70% and 75% at the throat were studied.

Stenosis Geometry

The geometry of the stenosis model is depicted in Fig. 6. A cosine function dependent on the axial coordinate, x, was used to generate the geometry shown. Following equations specify the shape of the stenosis

$$\begin{aligned} S(x) &= \frac{1}{2}D[1 - s_0(1 + \cos(2\pi x/L))], \\ y &= S(x)\cos\theta, \quad z = S(x)\sin\theta, \end{aligned} \tag{35}$$

where D denotes the diameter of the non-stenosed tube, $s_0 =$ 0.25, 0.3, 0.325, 0.35 and 0.375 for the 50%, 60%, 65%, 70% and 75% radius constriction, L is the length of the stenosis, and $x = 0$ is the location of the throat of the stenosis. For most cases, $L = 2D$. For the axially elongated stenosis, $L = 3D$.

Boundary and Initial Conditions

Waves reflected back from the boundaries may reduce the computational stability. Therefore the upstream and downstream boundaries are placed at $x = -10D$ and $x = 25D$, which are far away from the stenosis.

The parabolic velocity profile for laminar fully developed Poiseuille flow is imposed at the inlet

$$\frac{u}{u_i} = 2(1 - (2r/D)^2), \quad \frac{v}{u_i} = 0, \quad \frac{w}{u_i} = 0, \tag{36}$$

where u_i is the mean axial velocity at inlet and $r = \sqrt{y^2 + z^2}$ is the radial distance from the vessel centerline. The inlet density is fixed as $\rho = \rho_i$, where ρ_i is the initial density of the fluid which flows into the vessel. Since four eigenvalues of the governing equations are positive while one eigenvalue is negative for subsonic compressible flow, four conserved variables need to be given from upstream flow while one variable from downstream. In this study, the fluid density and flow velocities at the inlet are fixed (to ensure a constant mass flow rate), while the inlet pressure is extrapolated from the computational domain. The outlet pressure is kept as a constant as $p = p_o$ and the outlet velocity gradient along the streamwise direction is set to 0. Meanwhile, adiabatic no-slip boundary conditions are applied at vessel walls.

The initial density and pressure of the fluid is given as ρ_i and p_o everywhere. The initial axial velocity profile at any axial location is given as a parabola. The initial mean axial velocity of sections perpendicular to $x-$axis at non-stenosed locations ($x < -D$ and $x > D$) is given as u_i which is the mean axial velocity at the inlet. To ensure mass conservation, the initial mean axial velocity at stenotic locations ($-D \leq x \leq D$) is adjusted to guarantee conservation of mass across any sections perpendicular to $x-$ axis.

Non-dimensional Parameters

The key non-dimensional parameter of any vessel flow is its Reynolds number $Re = \rho u_i D/\mu$. All simulations are performed at $Re = 500$ based on the fact that the Reynolds number of blood flow is 400 in the human common carotid artery [18]. As have been discussed previously, to reduce the compressibility effects, we have to use small Mach numbers. More specifically, in this work, we have chosen a Mach number of 0.02 for all the cases.

Computational Meshes

The spatial discretization was based on N-th order SD method within K hexahedral elements. The total degree of freedom is KN^3.

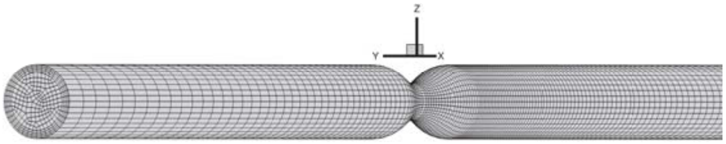

(a) CONFORMING MESH (OVERVIEW)

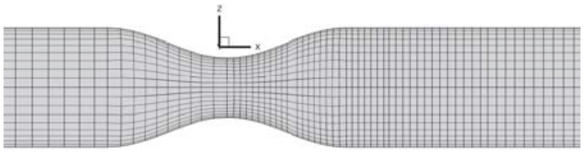

(b) CONFORMING MESH (SIDE VIEW)

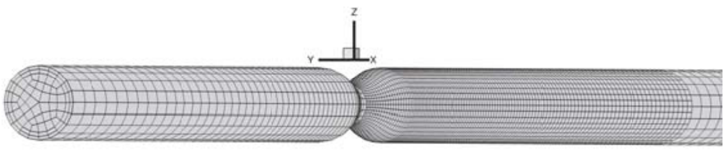

(c) NON-CONFORMING MESH (OVERVIEW)

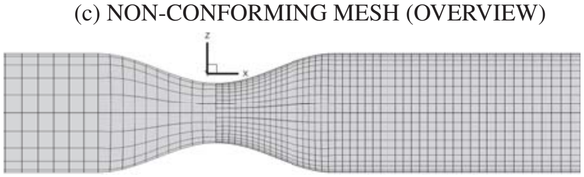

(d) NON-CONFORMING MESH (SIDE VIEW)

FIGURE 7: MESHES FOR STENOSIS OF 50% RADIUS CONSTRICTION

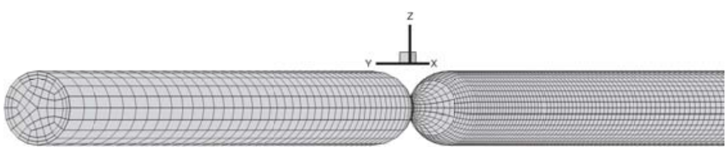

(a) NON-CONFORMING MESH (OVERVIEW)

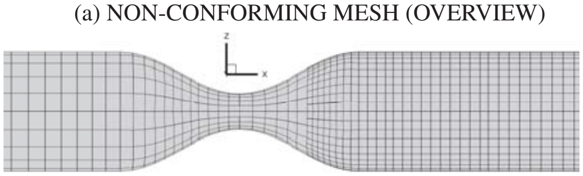

(b) NON-CONFORMING MESH (SIDE VIEW)

FIGURE 8: MESHES FOR STENOSIS OF 70% RADIUS CONSTRICTION

For verification, flows through stenosis of 50% radius constriction are simulated. Computations are first performed on a conforming mesh and a non-conforming mesh locally refined at post-stenotic region. For the conforming mesh in Fig. 7a, take any cross-section to view, 40 grid points are uniformly distributed in the circumferential direction and boundary layer mesh has 4 layers with 1.1 growth rate towards the centerline. Mesh along streamwise direction is doubled downstream of stenosis throat, as shown in Fig. 7b. The number of elements is 59470. For the non-conforming mesh, 20 grid points are placed in the circumferential direction with equal spacings. All computational elements located in the region where $0 \leq x \leq 10D$ are refined into 8 child elements, as shown in Fig. 7c and 7d. The number of elements for this mesh is 42000, which is smaller than that for the conforming mesh.

For cases whose radius constriction is bigger than 60%, the CFL constraint at stenosis throat is severe since the sizes of computational elements there are extremely small. This limits the global computing efficiency. Take the case of 70% radius constriction to illustrate the point. To solve the problem, all computational elements downstream of $x = 0.58D$ are refined while the upstream mesh remains coarse, as shown in Fig. 8. This technique allows us to perform all simulations at the same size of time step.

For all simulations, a fifth order ($N = 5$) SD scheme is used, which corresponds to approximately 7 million degrees of freedom.

VERIFICATION AND VALIDATION

Comparison with DNS and Experimental Data

The non-dimensional pressure is defined as $p^* = (p - p_o)/(\frac{1}{2}\rho_i u_i^2)$. In the simulation of flow through 50% radius constriction, the criterion for convergence of solution is that the fluctuation of non-dimensional inlet pressure $p_i^* = (p_i - p_o)/(\frac{1}{2}\rho_i u_i^2)$ is less than 0.1. After $tu_i/D = 45$, the computation converges as shown in Fig. 9. Non-dimensional $z-$vorticity and axial velocity contour in Fig. 11 show a laminar axisymmetric jet and shear layer. The highest $z-$vorticity is located at the throat wall and its immediate downstream region. Axial velocity profiles at four axial locations downstream of the stenosis are compared with DNS results from [3] and digitized experimental results from [4], as shown in Fig. 10. Profiles predicted from SD solver agree well with DNS profiles from [3], although both profiles from numerical computation are not always consistent with experimental data. The difference lies at the downstream side where numerical computation predicts a long recirculation region near the wall while experiments predict a not completely laminar flow and reattachment point not that far away. From Fig. 11a, the reattachment point predicted from SD solver is approximately $x \approx 11D$, which is exactly the same as previous DNS prediction.

Mesh Independency Study

Another simulation of flow past stenosis of 50% radius constriction at $Re = 500$ is conducted with a non-conforming mesh presented in Fig. 7c and 7d. No discontinuity is witnessed at the non-conforming interfaces $x = 0$ and $x = 10D$ in plots of

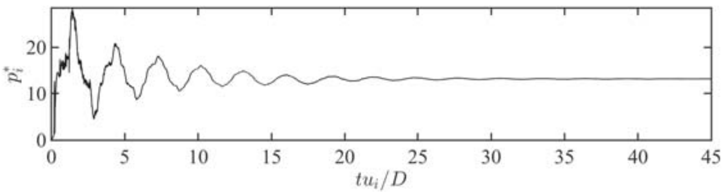

FIGURE 9: NON-DIMENSIONAL INLET PRESSURE WITH RESPECT TO NON-DIMENSIONAL TIME

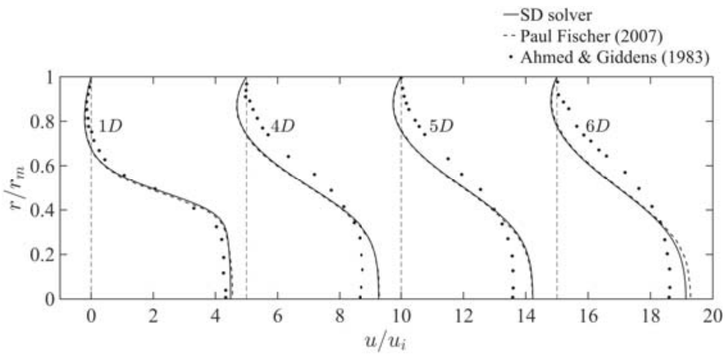

FIGURE 10: COMPARISON OF AXIAL VELOCITY PROFILES AT DOWNSTREAM LOCATIONS WITH DNS AND EXPERIMENTAL PROFILES FOR STEADY FLOW THROUGH THE STENOSIS OF 50% RADIUS CONSTRICTION. THE AXIAL LOCATIONS ARE INDICATED IN TERMS OF THE DISTANCE DOWNSTREAM FROM THE STENOSIS THROAT

streamlines and variable contours, which means that the non-conforming interface does not contaminate the computation, as shown in Fig. 12. At all axial locations, the relative difference between velocity profiles obtained with conforming and non-conforming meshes is less than 0.1%.

RESULTS AND DISCUSSION

The Q-criterion [19] is used in this study for the visualization and analysis of coherent flow structures. For the stenosis of 50% radius constriction, figure 13a shows that the shape of the iso-surface of Q-criterion is like a torus close to the wall of the stenosis throat and there are no vortical structures downstream of the throat which have similar amount of strength as those located at the stenosis throat. With degree of radius constriction increasing to 60% and above but below 75%, vortex rings start to develop downstream the throat, as shown in Fig. 13b-d. These vortex rings seem to have a equidistant arrangement. They are advecting downstream before they feel the restriction exerted by the vessel walls. They finally merge into a large area of turbulence and break down into chaotic vortical structures. The distances that vortex rings can advect downstream decrease when the stenosis constriction becomes more and more critical. For stenosis of 60%, 65% and 70% radius constriction with $L = 2D$, the vortex rings can remain intact until approximately $x = 7D$, $x = 5D$ and $x = 3D$. For 70% radius constriction, the advection distance of vortex rings for the stenosis of $L = 2D$ does not vary a lot compared with that for the axially elongated stenosis of $L = 3D$, as shown in Fig. 13d and 13e. Meanwhile, the pressure drops in these two cases are similar. This may imply that the flow structures of post-stenotic regions are not quite dependent on the aspect ratio of the stenosis. When the degree of radius constriction turns to 75%, the flow through stenosis becomes unstable immediately downstream the throat and is characterized by a dramatic increase of pressure drop, as shown in Fig. 13f. All simulation results show that the flow through stenosis is extremely sensitive to the degree of radius constriction of the stenosis.

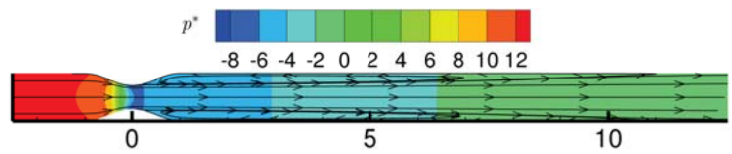

(a) NON-DIMENSIONAL PRESSURE CONTOUR AND PLOTS OF STREAMLINES

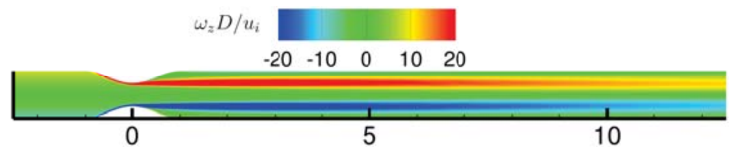

(b) NON-DIMENSIONAL $z-$VORTICITY CONTOUR

FIGURE 11: FLOW FIELD AT FINAL STEADY STATE FOR 50% RADIUS CONSTRICTION STENOSIS

Figure 14 shows that shear layers are formed, rolled up and advected downstream between the central jet and the recirculation region. When fluid ejected from the throat with high speed meets with slow fluid downstream close the vessel walls, the classical Kelvin-Helmholtz instability develops. This implies that flow unsteadiness is primarily caused by the breakdown of Kelvin-Helmholtz-type vortices since unstable modes grow as these vortices advect downstream. Moreover, the axial distance that the vortices can remain stable are consistent with the distance that the vortex rings can advect downstream.

Figure 15 shows variation of pressure with axial coordinate. The non-dimensional pressure at $x = -L/2$ where area of the vessel starts to shrink is denoted as p_1^*. Pressure at other axial locations is evaluated as the difference between local pressure and p_1^*. For unsteady cases, mean pressure is shown, which is obtained from time average of instantaneous pressure. The pressure drops rapidly with increase of the degree of the stenosis,

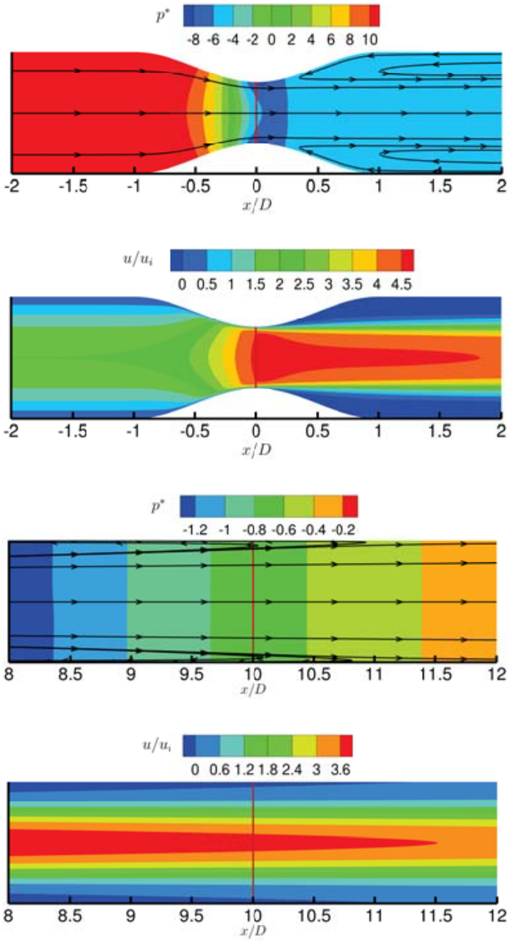

FIGURE 12: CONTOURS OF VARIABLES AND PLOTS OF STREAMLINES NEAR THE MORTAR INTERFACE AT $x = 0$ AND $x = 10D$ FOR STENOSIS OF 50% RADIUS CONSTRICTION. (RED LINES ARE MORTAR INTERFACES)

as shown in Fig. 15. For all cases, the pressure drops to a lowest point near approximately $2x/L = 0.08$ and then recover to a specific value p_2^*. For stenoses of 70 degree radius constriction, the lowest pressure near the throat for the stenosis of $L = 2D$ is a little lower than that for the stenosis of $L = 3D$. But there is nearly no difference between the pressure drop for both stenosis models, where pressure drop across a stenosis is defined as $\Delta p^* = p_1^* - p_2^*$. Area ratio is defined as the ratio of non-stenosed area A_1 to minimum area at the throat of the stenosis A_s. Figure 16 shows a strong linear correlation between the pressure drop and square of the area ratio with a linear correlation coefficient equal to 0.9998, just as reported in [8]. This linear relation exists even when the post-stenotic flow has turned into unsteady.

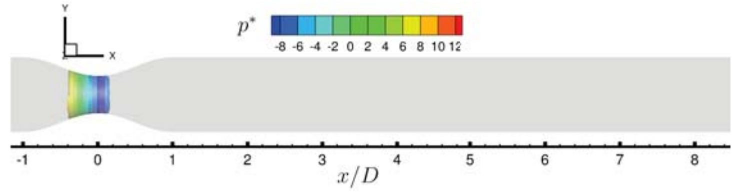

(a) STENOSIS OF 50% RADIUS CONSTRICTION

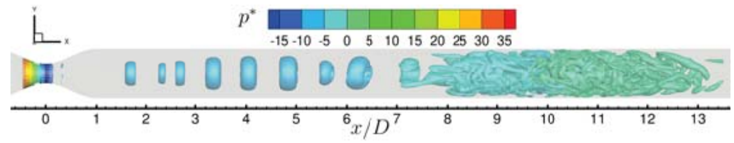

(b) STENOSIS OF 60% RADIUS CONSTRICTION

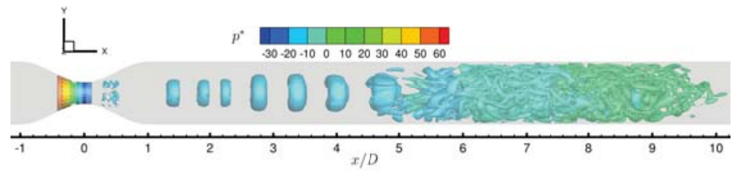

(c) STENOSIS OF 65% RADIUS CONSTRICTION

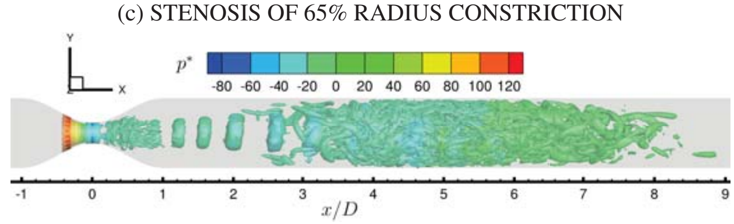

(d) STENOSIS OF 70% RADIUS CONSTRICTION

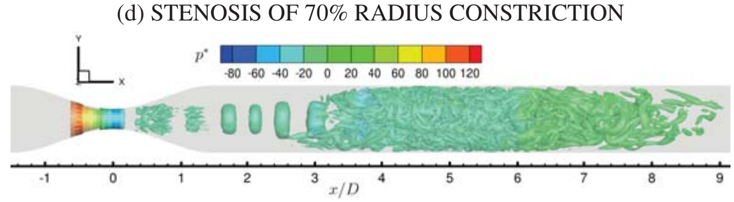

(e) AXIALLY ELONGATED STENOSIS OF 70% RADIUS CONSTRICTION ($L = 3D$)

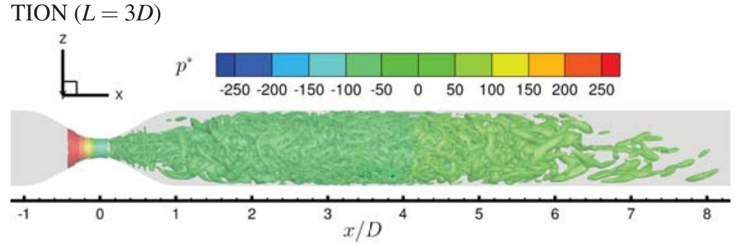

(f) STENOSIS OF 75% RADIUS CONSTRICTION

FIGURE 13: ISO-SURFACES OF NON-DIMENSIONAL Q-CRITERION (COLORED BY p^*). Q-CRITERION EQUAL TO 20 EXCEPT THAT Q-CRITERION EQUAL TO 5 FOR STENOSIS OF 60% RADIUS CONSTRICTION

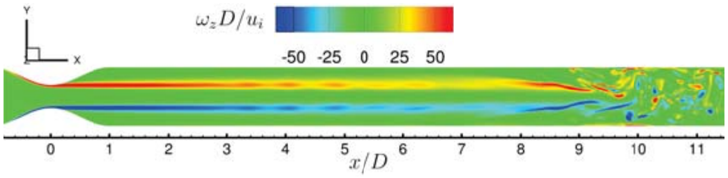

(a) STENOSIS OF 60% RADIUS CONSTRICTION

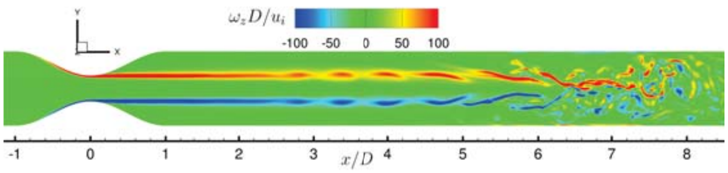

(b) STENOSIS OF 65% RADIUS CONSTRICTION

FIGURE 14: NON-DIMENSIONAL $z-$VORTICITY CONTOUR

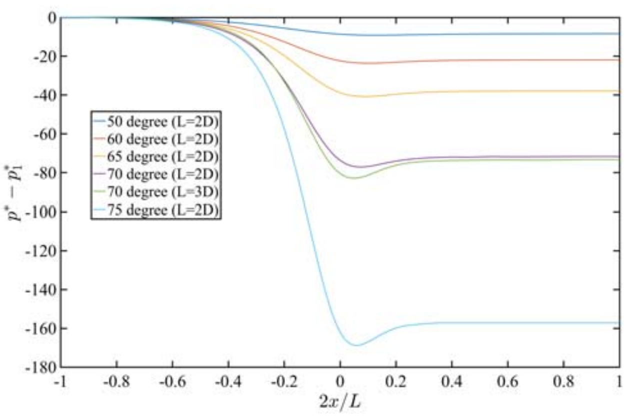

FIGURE 15: VARIATION OF NON-DIMENSIONAL PRESSURE WITH RESPECT TO AXIAL COORDINATE WITHIN RANGE OF THE STENOSIS

Parallelization for Meshes of Multi-level Refinement

Figure 18a shows the $z-$vorticity computed with the mesh presented in Fig. 8. Although the Kelvin-Helmholtz instability is clear, the vorticity contour in the region $3.18D \leq x \leq 5.84D$ shows that computation with the mesh cannot resolve the turbulence generated there. Then a new mesh which is locally refined not only at downstream of $x = 0.58D$ but also at the region $3.18D \leq x \leq 5.84D$ is generated, as shown in Fig. 17. The $z-$vorticity computed with the new mesh shown in Fig. 18b shows finer vortical structures at the region $3.18D \leq x \leq 5.84D$. And again no discontinuity is witnessed near mortar interfaces even if flow is characterized by strong turbulence and mixing

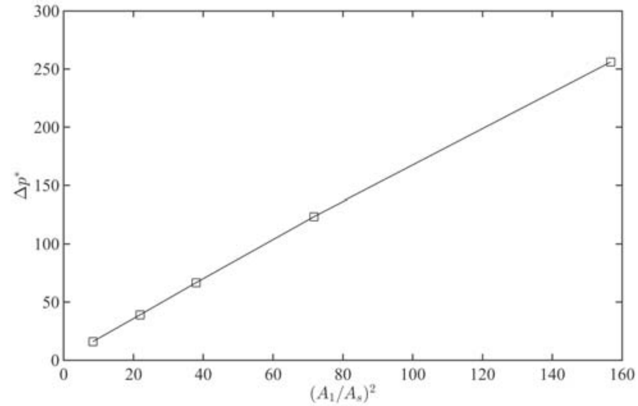

FIGURE 16: VARIATION OF NON-DIMENSIONAL PRESSURE DROP WITH SQUARE OF THE AREA RATIO

FIGURE 17: NEW MESH OF 3 LEVELS OF REFINEMENT (RED LINES DENOTE MORTAR INTERFACES)

layer.

For computations with meshes of multi-level refinements, whether a solver preserves good scalability is an important standard to evaluate the performance of the solver. Here, procedures to do parallel computing are introduced.

During preprocessing, an original coarse conforming mesh is refined into a non-conforming mesh of multiple levels. After refinement, we collect the mortar-to-vertex connectivity into a single file. For each mortar, the vertices that form its corresponding parent and child faces are stored in this file. Meanwhile, the refinement generates a new non-conforming mesh file where the elements are numbered consecutively. The Metis library [20] is then called to partition this mesh file. After that, each processor reads in its own part of the mesh. For example, figure 19 shows the partitions of a non-conforming mesh for six processors. For simplicity, only partitions for the first 3 processors are depicted. In order to see processor interfaces clearly, 3 partitions of the mesh are translated a little to set them apart. Then each processor reads in the global mortar-to-vertex connectivity. Note that each mortar is associated with 1 parent face and 1 child face. We call a mortar as local mortar if both faces associated with it fall in the partition for a single processor. Other mortars whose parent and child faces belong to different processors are called mortars on processor interfaces. For local mortars, exchange of information is also local and implementation of mortar algorithm is straightforward. For mortars on the processor interfaces, only

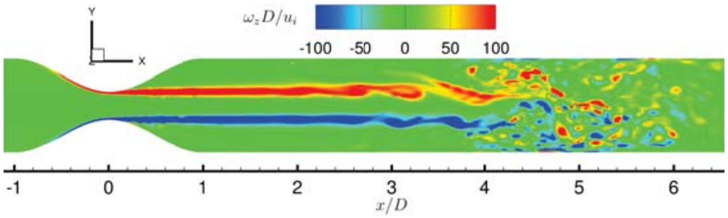

(a) FROM PREVIOUS MESH OF 2 LEVELS OF REFINEMENT

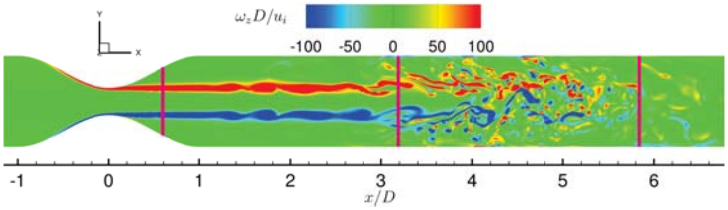

(b) FROM NEW MESH OF 3 LEVELS OF REFINEMENT (RED LINES DENOTE MORTAR INTERFACES)

FIGURE 18: NON-DIMENSIONAL $z-$VORTICITY CONTOUR FOR STENOSIS OF 70% RADIUS CONSTRICTION

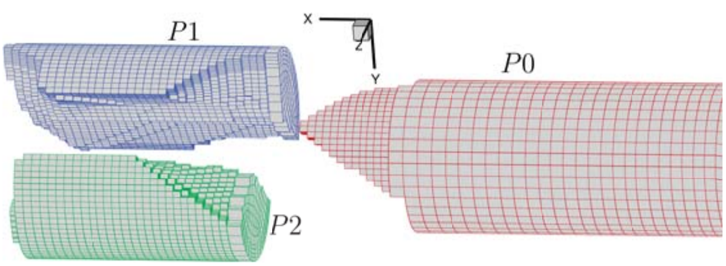

FIGURE 19: SCHEMATIC OF PARTITIONS OF A MESH OF 3-LEVELS OF REFINEMENT AT THE MORTAR INTERFACE LOCATED AT $x = 3.18D$ FOR 6 PROCESSORS

one side information is available locally and another side needs to be sent from its pairing face on a remote processor. A local mortar finds its pairing face by the global mortar-to-vertex connectivity. Once the pairing is done, it does not need to be updated since current mesh refinement is static. Since one mortar on the processor interface introduces only a very small amount of computational cost compared with cost inside each element, the overall load balancing is not a problem. Figure 20 shows the scalability curves for different orders of SD method with non-conforming interfaces treatment. It is noticed that the scalability improves as the scheme order (denoted by N) increases. This is consistent with the fact that the computational cost on each processor is of $O(N^3)$, whereas the communication cost is of $O(N^2)$ [21].

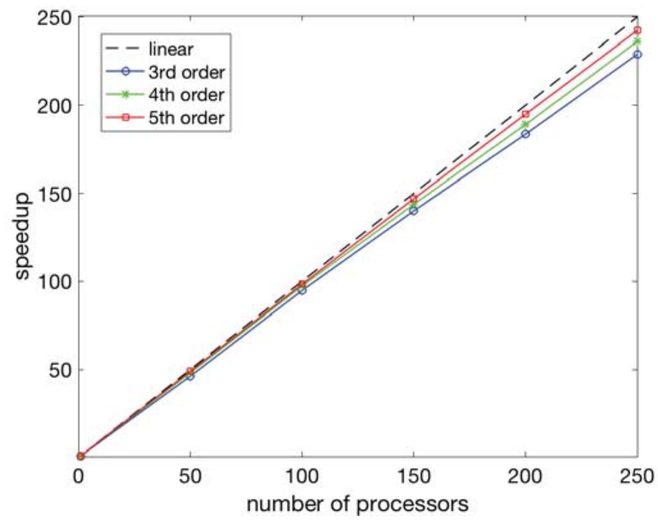

FIGURE 20: SPEEDUP OF THE SOLVER

CONCLUSIONS

A 3D parallel high-order SD solver with local mesh refinement capability is presented in this paper for unstructured high-order non-conforming grids. This solver uses high-order curved mesh in the vicinity of arterial wall and thus represents the geometries much more accurate than linear meshes employed in traditional solvers based on the finite volume method, such as ANSYS Fluent and STAR-CCM. Meanwhile, the local mesh refinement technique significantly reduces the overall computational cost by distributing more elements in critical regions, such as the post-stenotic region where the flow is characterized by large recirculation and development of shear layer instabilities. Rigorous verification and validation studies are performed by simulation of flow through a stenosis of 50% radius constriction at $Re = 500$ and comparing the velocity profiles obtained from the SD solver against previous DNS results and experimental data. Meanwhile, the variable contours with the non-conforming mesh shows that the watertight curved mortar algorithm does not contaminate the computation. Then simulations of stenoses of larger radius constriction are conducted. The post-stenotic flow starts to transition and become unsteady. An array of vortex rings is advecting downstream and remains intact until they hit the vessel walls. The longest distance that these vortex rings can travel downstream decreases as the radius constriction increases until the vortex rings break down at immediate downstream of stenosis throat for stenosis of 75% radius constriction and strong turbulence is produced which is characterized by dramatic pressure drop. This verifies that the clinical definition of critical stenosis is reasonable from the perspective of fluid mechanics. Moreover, the vorticity contours show the development of Kelvin-Helmholtz instability when shear layers were formed, rolled up and advected downstream between the central jet and the recirculation region. This implies that the unsteadiness is primarily caused by the breakdown of Kelvin-Helmholtz-type vortices since unstable modes grow as these vortices advect downstream. The axial location where the Kelvin-Helmholtz-type vortices start to break down is consistent with the distance that the vortex rings can travel downstream and remain intact. This distance will not change much when the aspect ratio of the stenosis changes, which implies that the distance is extremely sensitive to radius constriction, but not quite relevant to aspect ratio of the stenosis. Furthermore, the pressure drop proves to be linearly proportional to the square of the area ratio with a linear correlation coefficient equal to 0.9998. This relation remains valid even when the post-stenotic flow turns into unsteady for stenoses of large area reduction. Finally, the excellent scalability of the SD solver with multi-level refinement is proven.

ACKNOWLEDGMENT

The first author would like to give many thanks to Clarkson University and the Department of Mechanical and Aeronautical Engineering for financial support.

REFERENCES

[1] Ku, D., 1997.“Blood flow in arteries,” Annual Review of Fluid Mechanics, **29**, pp. 399-434.

[2] Klabunde, R., 2018. “Critical stenosis,” Cardiovascular physiology concepts, from https://www.cvphysiology.com/Hemodynamics/H008

[3] Varghese, S., Frankel, S., Fischer, P., 2007. “Direct numerical simulation of stenotic flows. Part 1. Steady flow,” Journal of Fluid Mechanics, **582**, pp. 253-280.

[4] Ahmed, S., Giddens, D., 1983. “Velocity measurements in steady flow through axisymmetric stenoses at moderate Reynolds numbers,” Journal of Biomechanics, **16**(7), pp. 505-507.

[5] Sherwin, S.J., Blackburn, H.M., 2005. “Three-dimensional instabilities and transition of steady and pulsatile axisymmetric stenotic flows,” Journal of Fluid Mechanics, **533**, pp. 297-327.

[6] Varghese, S., Frankel, S., Fischer, P., 2007. “Direct numerical simulation of stenotic flows. Part 2. Pulsatile flow,” Journal of Fluid Mechanics, **582**, pp. 281-318.

[7] Jain, K., 2020. “Transition to turbulence in an oscillatory flow through stenosis,” Biomechanics and Modeling in Mechanobiology, **19**, pp. 113-131.

[8] Seeley, B.D., Young, D.F., 1976. “Effect of geometry on pressure losses across models of arterial stenoses,” Journal of Biomechanics, **9**(7), pp. 439-446.

[9] Rusanov, V., 1961.“Calculation of interaction of non-steady shock waves with obstacles,” Journal of Computational and Mathematical Physics USSR, **1**, pp. 267–279.

[10] Liang, C., Jameson, A., Wang, Z., 2009. “Spectral difference method for compressible flow on unstructured grids with mixed elements,” Journal of Computational Physics, **228**(8), pp. 2847-2858.

[11] Kopriva, D.A., 1998. “A staggered-grid multidomain spectral method for the compressible navier-stokes equations,” Journal of Computational Physics, **143**, pp. 125–158.

[12] Sun, Y., Wang, Z., and Liu, Y., 2007. “High-order multidomain spectral difference method for the navier-stokes equations on unstructured hexahedral grids,” Communication in Computational Physics, **2**, pp. 310–333.

[13] Ruuth, S., 2006. “Global optimization of explicit strong-stability-preserving Runge-Kutta methods,” Mathematics of Computation, **75**, pp. 183-207.

[14] Kopriva, D.A., 1996. “A conservative staggered-grid Chebyshev multidomain method for compressible flows II. A semi-structured method,” Journal of Computational Physics, **128**(2), pp. 475-488.

[15] Zhang, B., Liang, C., 2015. “A simple, efficient, and high-order accurate curved sliding-mesh interface approach to spectral difference method on coupled rotating and stationary domains,” Journal of Computational Physics, **295**, pp. 147-160.

[16] Zhang, B., and Liang, C., “A high-order sliding-mesh spectral difference solver for simulating unsteady flows around rotating objects,” 31st Symposium on Naval Hydrodynamics, Monterey, CA, 2016.

[17] Kopriva, D.A., Hindenlang, F.J., Bolemann T., Gassner, G.J., 2019. ”Free-stream preservation for curved geometrically non-conforming discontinuous Galerkin spectral elements,” Journal of Scientific Computing. **79**, pp. 1389-1408.

[18] Ghalichi, F., Deng, X., De Champlain, A., Douville, Y., King, M., and Guidoin, R., 1998. “Low Reynolds number turbulence modeling of blood flow in arterial stenoses,” Biorheology. **35**(4&5), pp. 281-294.

[19] Hunt, JC., Wray, A., Moin, P., 1988. “Eddies, streams, and convergence zones in turbulent flows,” Center for Turbulence Research Report CTR-S88, **1**, pp. 193-208.

[20] Karypis, G., Kumar, V., 1999. “A fast and high quality multilevel scheme for partitioning irregular graphs,” SIAM Journal on Scientific Computing, **20**(1), pp. 359-392.

[21] Zhang, B., Liang, C., Yang, J., Rong, Y., “A 2D parallel high-order sliding and deforming spectral difference method,” Computers and Fluids, **139**(5), pp. 184-196.